Materials Advances

ROYAL SOCIETY OF CHEMISTRY

PAPER

View Article Online
View Journal | View Issue

Cite this: *Mater. Adv.*, 2024, 5, 9744

Unveiling the synergic potential of dual junction $MoSe_2$/n-Ga_2O_3/p-GaN heterojunctions for ultra-broadband photodetection†

Vishnu Aggarwal, [abc] Manish Kumar, [d] Rahul Kumar,[ab] Sudhanshu Gautam,[ab] Aditya Yadav,[ab] Shikha Shrivastava,[ab] Anjana Dogra,[ab] Govind Gupta,[ab] Sumeet Walia [c] and Sunil Singh Kushvaha *[ab]

For practical optoelectronic applications, photodetectors capable of detecting light across a wide wavelength range (200–1100 nm) are essential. Heterojunction semiconductors play a crucial role in developing such multi-wavelength photodetectors. In particular, the heterojunction of transition metal chalcogenides (tuneable bandgap and high electron mobility) and Ga_2O_3 (wide bandgap of >4 eV) is a significant research topic for photodetector fabrication exhibiting an ultrawide spectral photodetection capability. In this study, epitaxial β-Ga_2O_3 thin films were grown on atomically flat sapphire (0001) and p-GaN/sapphire (0001) surfaces using a pulsed laser deposition technique. The effect of the substrate on the crystalline, optical, electronic, and photoresponse properties of β-Ga_2O_3 thin films was thoroughly investigated and correlated with theoretical insights from density functional theory. To achieve broadband photodetection, a heterojunction of $MoSe_2$ and the as-grown Ga_2O_3 films was fabricated, enabling light detection from the deep ultraviolet (UV) to the near-infrared (NIR) spectral regions. The $MoSe_2$/Ga_2O_3/p-GaN device exhibited an expanded detection range from deep ultraviolet (240–320 nm) to long-wavelength ultraviolet (320–400 nm) and a significant responsivity of 5.5 A W^{-1} in the NIR region, nearly fourfold higher than that of the $MoSe_2$/Ga_2O_3/sapphire device. These results highlight the potential of these hybrid structures for developing multi-wavelength photodetectors with high photoresponse across the deep-UV to NIR spectral regions, offering promising applications in fields ranging from environmental monitoring to communications.

Received 17th September 2024,
Accepted 8th November 2024

DOI: 10.1039/d4ma00934g

rsc.li/materials-advances

Introduction

Deep ultra-violet (DUV) photodetectors (PDs) are increasingly in demand because the Earth's ozone layer absorbs UV-C light (200–280 nm), preventing it from reaching its surface. This characteristic results in low background noise, making these PDs valuable for applications in military and civilian fields, including in flame sensing, missile tracking, biomedicine, and secure optical communication.[1–4] Traditional DUV PDs based on Si and GaAs often require optical filters and high-power supplies, which add to their bulk in terms of size and cost. As a result, there is growing interest in using ultra-wide-bandgap (UWBG) semiconductors with bandgaps greater than ~4 eV, such as diamond, β-Ga_2O_3, MgZnO, AlGaN, and h-BN, for DUV PD fabrication.[5–9] However, diamond and BN are typically limited to vacuum UV detection, while heavy doping in MgZnO and AlGaN can induce phase variations and increase defect density, limiting their utility in optoelectronics.[10–12]

In contrast, Ga_2O_3 is an ideal choice for DUV PDs due to its direct and UWBG of 4.4–5.0 eV, high breakdown electric field (theoretical value ~8 MV cm^{-1}), chemical robustness, and radiation hardness.[6,13–15] The n-type semiconductor properties in Ga_2O_3 primarily arise from intrinsic oxygen deficiencies. However, creating a p–n homojunction in Ga_2O_3 is challenging due to the difficulty in achieving p-type doping.[13–15] To fully harness the potential of β-Ga_2O_3, an alternative approach involves creating p–n heterojunctions by integrating Ga_2O_3 with other p-type wide-bandgap (WBG) semiconductors, such as SiC,

[a] *CSIR-National Physical Laboratory, Dr K. S. Krishnan Road, New Delhi 110012, India. E-mail: kushvahas@nplindia.org*
[b] *Academy of Scientific and Innovative Research (AcSIR), Ghaziabad 201002, India*
[c] *School of Engineering, RMIT University, Melbourne, Victoria 3000, Australia*
[d] *Physics Department and CSMB, Humboldt-Universität zu Berlin, Zum Großen Windkanal 2, 12489 Berlin, Germany*

† Electronic supplementary information (ESI) available: RHEED, AFM images of Ga_2O_3 [Fig. S1], PL and XPS of Ga_2O_3 and p-GaN templates [Fig. S2], DFT partial density of states in Ga_2O_3 [Fig. S3], photodetector characteristics of bare Ga_2O_3 [Fig. S4], AFM, XPS, and *I–V* characteristics of $MoSe_2$/Ga_2O_3 [Fig. S5–S7]. Table S1 contains the peak positions of XPS spectrum $MoSe_2$/Ga_2O_3 samples. See DOI: https://doi.org/10.1039/d4ma00934g

GaN, NiO, and CuSCN. Integrating these WBG semiconductors with Ga_2O_3 not only enhances the photodetection properties of Ga_2O_3-based photodetectors but also expands the wavelength range of UV photodetection.[16–19] Among these semiconductors, GaN stands out as a promising candidate for integration with Ga_2O_3 to develop highly efficient solar-blind photodetectors. This is due to the low lattice mismatch between the (002) plane of GaN and the (−201) plane of Ga_2O_3, along with GaN's superior physical properties, such as its direct bandgap of 3.4 eV, a low excitonic binding energy of approximately 25 meV, and high electron mobility.[20,21] Furthermore, in recent years, van der Waals (vdW) heterojunctions have gained significant attention due to their exceptional properties, including enhanced conductivity, wide-spectrum light absorption, and high carrier mobility.[22–25] Furthermore, the vdW heterojunction of Ga_2O_3 with two-dimensional (2D) transition metal dichalcogenides (TMDs) semiconductors is a significant research topic for photodetector fabrication exhibiting broad spectral photoresponse capability.[26,27] However, the vdW heterojunction of MoS_2 and Ga_2O_3 has mostly been explored. In contrast, superior carrier mobility and a narrower band gap of $MoSe_2$ than MoS_2 can be advantageous for ultrawide photodetection, including visible to near-infra-red (NIR) regions.[28,29]

In this study, we have systematically investigated the photoresponse capability of single and dual junction photodetectors for ultrawide spectral photodetection (p–n junction: n-Ga_2O_3/p-GaN and vdW heterojunction: $MoSe_2/Ga_2O_3$). Ga_2O_3 was grown on pristine sapphire (0001) and p-GaN/sapphire at 750 °C using the pulsed laser deposition (PLD) technique. High-resolution X-ray diffraction (HRXRD) 2θ–ω scans confirmed the formation of the β-phase of Ga_2O_3 on both substrates. Furthermore, the crystalline, structural, optical, and electronic properties of PLD grown β-Ga_2O_3 are elucidated, and outcomes are correlated with theoretical study *via* density functional theory (DFT) calculations. The photoresponse study of as-grown Ga_2O_3 was performed by fabricating metal–semiconductor–metal (MSM) type photodetector devices. Furthermore, a magnetron-sputtered $MoSe_2$ thin film was decorated with Ga_2O_3/sapphire and Ga_2O_3/p-GaN/sapphire to explore the photoresponse properties of single and dual junction photodetectors. The resulting dual junction $MoSe_2$-decorated Ga_2O_3/p-GaN photodetector demonstrated significantly higher responsivity compared to the single junction, with values of 32.7, 25.2, and 5.5 A W^{-1} in the deep-UV (UV-C), UV-A, and NIR regions at an applied voltage of 10 V.

Experimental details

Many techniques have been used to grow Ga_2O_3 on GaN, such as the oxidation of GaN grown by metal–organic chemical vapor deposition (MOCVD) and molecular beam epitaxy (MBE), PLD, *etc.*[18,30–32] However, the oxidation method of GaN for Ga_2O_3 limits the choice of substrate whereas the MOCVD technique requires toxic precursors, and MBE has a slow and complex growth process. On the other hand, the PLD technique can be used to grow Ga_2O_3 on a number of substrates at relatively low temperatures and is easy to operate; hence, it is a versatile technique for the growth of Ga_2O_3. Here, we have grown Ga_2O_3 thin films using the PLD technique on two different substrates: atomically flat bare sapphire (0001) and p-GaN/sapphire (0001) templates at 750 °C and called them the GS and GT samples, respectively. The base pressure of the PLD chamber was 2×10^{-6} mbar. The PLD chamber is equipped with *in situ* reflection of high energy electron diffraction (RHEED). The chemical cleaning of samples was performed by ultra-sonication in acetone followed by isopropyl alcohol. The thermal cleaning of samples was performed at 800 °C and 760 °C in a PLD chamber for sapphire and p-GaN, respectively, for 30 min under a 6 N pure oxygen environment with an oxygen partial pressure of 6×10^{-2} mbar. The PLD target of Ga_2O_3 used was 99.99% pure and stoichiometric. The Ga_2O_3 target was ablated using a KrF excimer laser with a wavelength of 248 nm and a pulsed width of 25 ms. The oxygen pressure was maintained at 1.5×10^{-3} mbar, and the number of laser shots was 3000 at a laser energy density and repetition rates of ∼3 J cm^{-2} and 10 Hz, respectively. The growth of Ga_2O_3 was monitored using an equipped RHEED system at an operating voltage of 35 kV. After that, the $MoSe_2$ thin film was deposited on PLD-grown Ga_2O_3 samples using r.f. Magnetron sputtering having a base vacuum of $\sim 2 \times 10^{-7}$ mbar. The stoichiometry 4 N pure $MoSe_2$ target was used to deposit $MoSe_2$ thin films at a growth temperature and a pressure of 400 °C and $\sim 5 \times 10^{-3}$ mbar (using 6 N pure Ar gas), respectively, at an r.f. power of 100 W. Due to the difference in the volatility of Mo and Se, the deposited $MoSe_2$ thin film possesses Se deficiency. Therefore, to reduce the deficiency of Se, post-selenization of the $MoSe_2$/PLD-Ga_2O_3 thin film was carried out at 300 °C for 1 hour. The $MoSe_2$ thin film sample grown on Ga_2O_3/sapphire is called MGS, and that on Ga_2O_3/p-GaN is called MGT. The thickness of $MoSe_2$ was estimated to be ∼30 nm by a stylus profilometer. HR-XRD $2\theta - \omega$ scans were obtained to determine the crystal orientation of the Ga_2O_3 nanostructures (X-ray source: $CuK_\alpha 1$ and λ = 0.15406 nm). The structural quality of PLD-grown Ga_2O_3 was studied using room temperature Raman spectroscopy in backscattering mode using an Ar^+ laser (λ = 514.5 nm) as an excitation source. All the samples' surface morphology and roughness were investigated by atomic force microscopy (AFM) in tapping mode and field emission scanning electron microscopy (FESEM) at 25 kV operating voltage. Also, the stoichiometry of Bi_2Se_3 was estimated using energy dispersive spectroscopy (EDS) spectra. The room temperature photoluminescence (PL) spectroscopy technique was employed to examine the optical quality of the PLD-grown Ga_2O_3 (using a laser with λ = 213 nm). The core-level and valence band spectra of the Ga_2O_3 and $MoSe_2/Ga_2O_3$ samples were probed using the X-ray photoelectron spectroscopy (XPS) technique with an Al-K_α X-ray source. Furthermore, after the deposition of $MoSe_2$ thin films on PLD-Ga_2O_3 to make $MoSe_2/Ga_2O_3$/sapphire and $MoSe_2$/Ga_2O_3/GaN hybrid structures, we fabricated MSM PDs on these hybrid structures using Cr/Au metal electrodes of thickness 10/100 nm deposited using a thermal evaporation technique. A shadow mask was used to maintain the gap of ∼100 μm

between the two Cr/Au electrodes. The spectral photocurrent measurements were performed using a xenon lamp. A Keithley 2450 source meter was used to characterize these hybrid MSM PDs' photoresponse properties in UV (255 and 355 nm) and NIR regions (1064 nm). The transient photoresponse was studied with multiple ON–OFF cycles of 10 s under these laser illuminations at various externally applied biases of 0.1–10 V. The DFT[33,34] calculations were carried out within the generalized gradient approximation (GGA) in the PBESol[35] parameterization for exchange–correlation effects using FHI-aims,[36] which is an all-electron code with numerical atom-cantered basis sets [further computation details are included in the ESI†].

Result and discussion

The *in situ* RHEED pattern during the evolution of the PLD-grown Ga_2O_3 thin film is shown in Fig. S1(a)–(f) in the ESI,† which reveals that 3D Ga_2O_3 was grown on sapphire and p-GaN substrates. Furthermore, the surface texture and roughness of the Ga_2O_3 samples were examined using AFM, and the AFM images are shown in Fig. S1(g) and (h) (ESI†). The AFM image showed the granular morphology of the Ga_2O_3 thin film with root mean square roughness values of 7.29 and 4.28 nm for the GS and GT samples, respectively. The lower roughness value of the GT sample grown on p-GaN reveals its smoother surface compared with that grown on sapphire (0001).

Fig. 1(a) displays the HRXRD $2\theta - \omega$ scan results for the GS and GT samples in the 2θ range of 10 to 90°. The diffraction peaks for the GS sample were observed at positions of 18.90, 38.30, and 58.90°, corresponding to the (−201), (−402), and (−603) planes of Ga_2O_3, respectively.[37] Similarly, the XRD peaks for Ga_2O_3 in the GT sample were located at 2θ angles of 18.82, 38.20, and 58.94°, related to its (−201), (−402), and (−603) Ga_2O_3 crystal planes.[37–39] The XRD diffraction peaks are indexed using the JCPDS file 41–1103. It is clear from the $2\theta - \omega$ scan that the PLD-grown Ga_2O_3 has been grown in only one direction-oriented plane $\{-2n0n\}$, which indicates the formation of the β-Ga_2O_3 phase. It was determined that the oxygen arrangement on sapphire (0001) is equivalent to that on β-Ga_2O_3 (−201). As a result, this orientation is preferred.[40] The higher intensity and lower full width at half maximum (FWHM) of the Ga_2O_3 XRD peaks in the GT sample compared with those of the GS sample reveal the better crystalline quality of the GT sample.[37] Further, the peak at 41.2° in the $2\theta - \omega$ scan of both the GS and GT samples is related to the (0006) plane of the sapphire substrate. The additional peaks present in the $2\theta - \omega$ scan of the GT sample at 34.46 and 72.62° correspond to the (0002) and (0004) planes of GaN, respectively.[41]

Furthermore, to analyze the structural properties of PLD-grown Ga_2O_3, we performed Raman spectroscopic measurements ranging from 150 to 800 cm^{-1}, as shown in Fig. 1(b). The inset of Fig. 1(b) presents the magnified view of the Raman spectra of the GS and GT samples in the range of 150 to 400 cm^{-1}. The Raman spectrum in the inset reveals that the Raman peaks of the GS sample are located at Raman shifts of 171.4, 201.0, and 346.9 cm^{-1} and are attributed to the $A_g^{(2)}$, $A_g^{(3)}$, and $A_g^{(5)}$ characteristic phonon modes of Ga_2O_3, respectively, while the characteristic Raman peaks of Ga_2O_3 in the GT sample are located at 170.1, 201.1, and 348.9 cm^{-1}.[42,43] Furthermore, the peaks marked by an asterisk are related to the sapphire substrate.[42,43] In contrast, the additional peaks in the Raman spectrum of the GT sample are the characteristic phonon modes of GaN identified as E_2 (high), A_1 (TO), and A_1 (LO).[44] The intensity of the Raman peaks of the GT sample was higher than that of the GS sample peaks, which reveals its better structural quality than that of the GS sample.

Next, we performed PL spectroscopy measurements to study the optical properties of the PLD-grown Ga_2O_3 samples. Fig. 1(c) and (d) show the PL spectra in the 240 to 800 nm wavelength region of the PLD-grown Ga_2O_3 samples. Fig. 1(c) shows the PL spectrum of the GS sample, which determines the near band edge emission of Ga_2O_3 at a wavelength of 266 nm, which indicates that the optical band gap of the PLD-grown Ga_2O_3 on sapphire is ∼4.6 eV.[31] Similarly, the PL spectra of the GT sample are shown in Fig. 1(d), where the NBE emission of Ga_2O_3 occurred at 266 nm, revealing its band gap to be ∼4.6 eV. The quenching of the NBE peak intensity in the GT sample indicates reduced electron–hole overlap/recombination, confirming efficient charge carrier separation at the heterojunction interface.[31,45] Furthermore, defect-related overlapping peaks were observed in the PL spectrum of both Ga_2O_3 samples, deconvoluted using the Gaussian function. The PL emission peaks in the range from 400 to 650 nm are attributed to the recombination of electrons and holes trapped in an acceptor and donor band, which originates due to oxygen and gallium vacancies, respectively, and the emission band beyond 650 nm is due to self-trapped defects. These defects are considered the primary cause of the persistent photoconductance (PPC) effect in oxide-based PDs.[46–48] It was depicted from the deconvoluted peaks in the overlapped defect band that the area under the

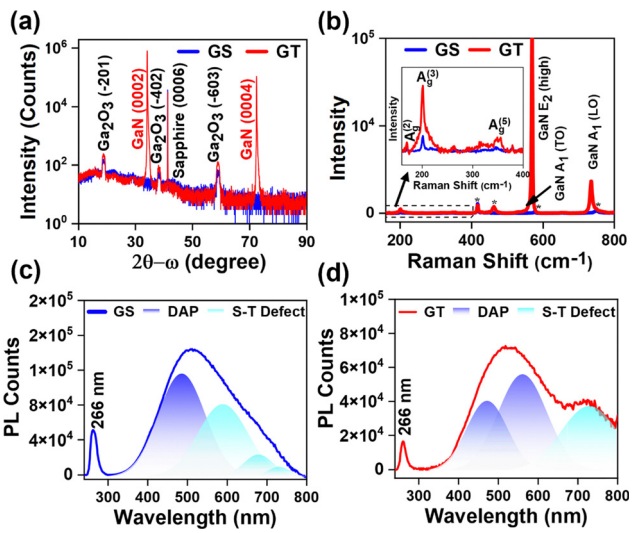

Fig. 1 (a) HR-XRD 2θ–ω scan and (b) Raman spectra of the GS (Ga_2O_3/sapphire) and GT (Ga_2O_3/p-GaN/sapphire) samples. (c) and (d) Fitted PL spectra of the GS and GT samples, respectively.

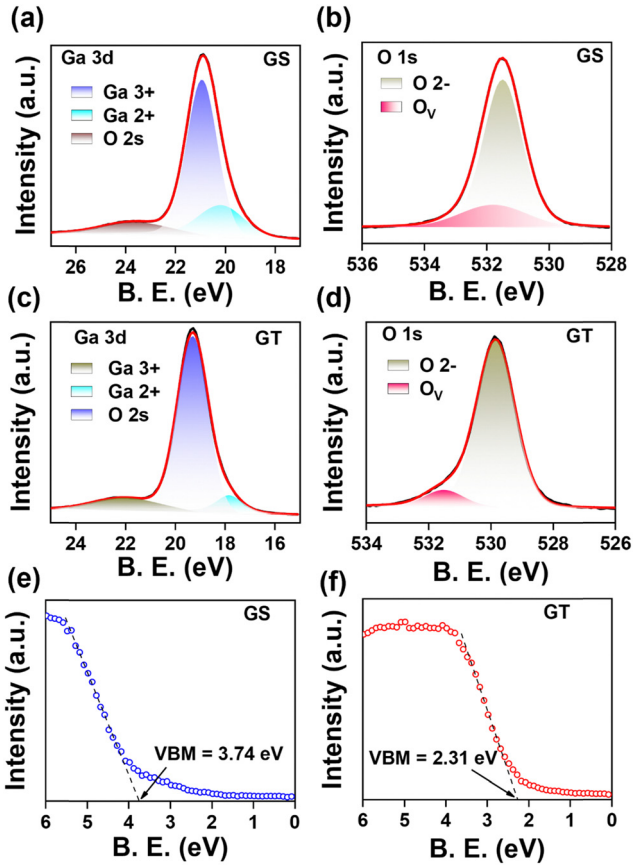

Fig. 2 XPS core level Ga 3d and O 1s scans of the (a) and (b) GS and (c) and (d) GT samples, and valence band spectra for the valence band maxima calculation of the (e) GS and (f) GT samples.

donor–acceptor pair (DAP) transition and self-trapped defects was estimated to be smaller in the GT sample compared to the GS sample. The lower intensity of the NBE peak and the lower area under the defect-related peaks in the GT sample convey its better quality than the GS sample. In addition, PL spectroscopy of the p-GaN template was performed, and the Voigt function fitted PL spectrum is shown in Fig. S2(a) (ESI†). The schematic of the energy band diagram for various transitions of electrons in the p-GaN template is shown in Fig. S2(b) (ESI†).

To study the chemical composition and valence states of elements on the surface of PLD-grown Ga_2O_3 films, we have performed an XPS core level scan on both samples, as shown in Fig. 2. The core level scan was deconvoluted using a mixed type of Gaussian–Lorentzian (Voigt) function, and the background was fitted using Sherley-type fitting. The core level Ga 3d spectrum of the GS sample is shown in Fig. 2(a) in the binding energy range of 17 to 27 eV. The Ga 3d spectrum is deconvoluted into three peaks at 20.19 eV, 20.92 eV, and 23.65 eV. The deconvoluted high-intensity peak at a binding energy of 20.92 eV is related to the Ga^{3+} chemical state, indicating a Ga–O bond associated with Ga_2O_3.[49,50] In comparison, a low-intensity peak at 20.19 eV reveals the presence of a Ga^{2+} chemical state due to its location in between the Ga^{3+} and Ga^{+} chemical states, whose binding energy lies at 20.3 eV and 19.3 eV.[49] In addition, a broad peak can be seen centered around the binding energy of 23.65 eV, which corresponds to the O 2s.[49,50] Furthermore, Fig. 2(b) shows that the O 1s scan was performed to analyze the oxygen binding states on the surface of PLD-grown Ga_2O_3/sapphire. The XPS O 1s core level spectrum was deconvoluted into two peaks: the peak centered at 531.49 eV is assigned to lattice oxygen with the O^{2-} chemical state associated with the metal–oxide bond, *i.e.*, in Ga_2O_3 while the peak at 531.77 eV corresponds to oxygen vacant bonds (O_V), specifically residual hydroxide species coupling with oxygen vacancies in Ga_2O_3.[47,49–51] Similarly, the Ga 3d core level spectrum of the GT sample has been fitted to three peaks at binding energies of 17.84 eV, 19.28 eV, and 22.02 eV, corresponding to Ga^{2+}, Ga^{3+} and O 2s chemical states, respectively, as shown in Fig. 2(c). Here also, the Ga^{3+} state and Ga^{2+} state indicate the formation of Ga–O bonds associated with Ga_2O_3 and GaO at the surface of Ga_2O_3 grown on p-GaN/sapphire (0001) using the PLD technique.[49,50] Furthermore, the XPS O 1s core level spectrum was analyzed by fitting it to two peaks [Fig. 2(d)]. The first peak, centered at 529.84 eV, is attributed to lattice oxygen with an O^{2-} chemical state associated with the metal–oxide bond in Ga_2O_3, and the second peak at 531.51 eV corresponds to oxygen vacant bonds, specifically residual hydroxide species coupling with oxygen vacancies in Ga_2O_3.[47,49–51] It was observed that the binding energy difference of Ga^{3+} and O^{2-} remained the same for both samples, which is 510.57 eV. In addition, two types of changes were observed in the XPS core-level scans of the GT sample when fitted with the same set of parameters as in core-level scans of the GS sample, except for the area of peaks, without introducing any additional component. First, the Ga_2O_3 component in the GT sample is likely higher than that of the GS sample as the relative ratio of the Ga^{3+} peak in the GT sample was estimated to be 85.39% compared to 78.25% in the GS sample [Table 1].

Table 1 Deconvoluted peak positions and their FWHM values for the XPS Spectra of GS and GT samples

XPS core level scan	Deconvoluted constituents	GS sample			GT sample		
		Binding energy (eV)	FWHM (eV)	Relative %	Binding energy (eV)	FWHM (eV)	Relative %
Ga 3d	Ga^{2+}	20.20	2.19	16.72	17.83	1.39	7.20
	Ga^{3+}	20.92	1.46	78.25	19.28	1.46	85.39
	O 2s	23.65	3.03	5.01	22.03	3.01	7.40
O 1s	O^{2-}	531.49	1.47	80.36	529.84	1.47	91.02
	O_v	531.77	2.53	19.63	531.51	1.48	8.97
E_{VBM}	—	3.74 eV			2.31 eV		

Second, the binding energy of both Ga^{3+} and O^{2-} peaks was lower than that of the GS sample, with a difference in the binding energy of 1.64 eV. The binding energy shift towards lower energy in the GT sample compared to the GS sample indicates that surface band bending (SBB) occurred in the GT sample with the introduction of p-GaN.[52] Additionally, the different energy shifts in the binding energy of the components of the O 1s core level scan (O^{2-} and O_V) were observed in both samples, which indicated the inhomogeneous SBB in the GT sample. Furthermore, the N 1s core level scans for the pristine p-GaN template and after the growth of Ga_2O_3 onto the p-GaN template, *i.e.*, the GT sample, are shown in Fig. S2(c) and (d) (ESI†) respectively. It can be noticed in Fig. S2(d) (ESI†), that the Auger signals diminished after the growth of Ga_2O_3. To further confirm the effect of SBB, we performed valence band spectra measurements on both the GS and GT samples. Fig. S2(e) (ESI†) shows the valence band spectra of the GS and GT samples in the 0–15 eV binding energy range. The valence band maxima (VBM) results from the hybridization of the O 2p and Ga 3d orbital.[53] The VBM for the GS and GT samples was estimated using the linear extrapolation method of the leading valence band edge, as shown in Fig. 2(e) and (f). The VBM was estimated to be 3.74 eV far from the Fermi level in the GS sample, as shown in Fig. 2(e), whereas, in the GT sample, it is only 2.31 eV far from the Fermi level [Fig. 2(f)]. The downward shift in the VBM of the GT sample by 1.53 eV, like that observed from the Ga 3d and O 1s core level scan, confirms the occurrence of SBB in Ga_2O_3 grown on p-GaN as compared to that grown on sapphire (0001).

Also, the valence band spectrum of pristine p-GaN was obtained as shown in Fig. S2(f) (see the ESI†), and the VBM was estimated to be 0.64 eV. As deduced from the PL spectra in Fig. 1(c) and (d), both PLD-grown Ga_2O_3 GS and GT samples have an energy band gap of $\sim$4.6 eV. It was surprisingly noticed from the valence band spectra that PLD-Ga_2O_3 grown on sapphire (0001) reveals (E_{VBM} = 3.74 eV) unintentionally doped (UID) high n-type (n^{++}) characteristics while that grown on p-GaN/sapphire (0001) [E_{VBM} = 2.31 eV] reveals a very low UID n-type (n^{--}) character.

To understand the role of the substrate in changing the optical and electronic states of Ga_2O_3 theoretically, DFT calculations were performed, and the results obtained are presented in Fig. 3. The computational details of the DFT calculations are presented in the ESI.† The atom projected partial density of states (pDOS) of pristine and defective Ga_2O_3 with single O-vacancy and *N*-substitution have been plotted as shown in Fig. 3(b)–(d), respectively. In pristine Ga_2O_3, the O-orbitals predominantly contribute to the valence band states, whereas Ga-orbitals contribute to the conduction band states (see Fig. 3(b)). The Fermi level is near the conduction band. In reality, some defects, for instance O-vacancies and N-related defects, might be present unintentionally due to the use of different substrates (here, GaN). With the creation of a single O-vacancy in the Ga_2O_3 supercell, some defect states appear near the valence band, leading to a decrease in the band gap. This result corroborates our experimental findings of PL

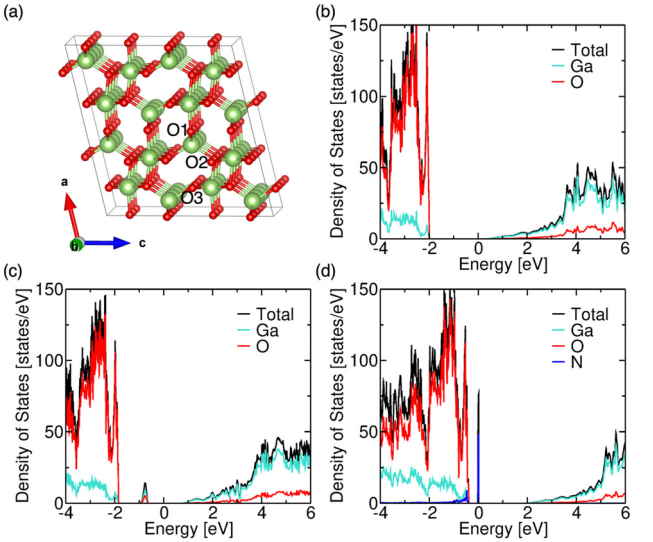

Fig. 3 (a) Crystal structure of Ga_2O_3. Atom projected partial density of states of (b) pristine, (c) O-vacant (O-vacancy at the O3-site), and (d) *N*-substituted Ga_2O_3 (*N*-substitution at the O3-site).

measurement, as shown in Fig. 1(c) and (d). These defect states are contributed by both O- and Ga-orbitals (see Fig. 3(c)). The decrease varies across three inequivalent O-sites (see Fig. 3(a) for inequivalent O-sites). The pDOS for the same is shown in Fig. S3(a) and (b) (ESI†). These localized states efficiently trap the minority charge carriers (holes), enhancing the photo-generated charge carriers' separation and recombination time. This leads to persistent photoconductivity in Ga_2O_3. However, when N is substituted at this site (which was previously O-vacant), the localized states, contributed by N-orbitals, move towards the VBM (see Fig. 3(d)) and appear at the VBM in the case of different N-sites (Fig. S3(c) and (d), ESI†). Hence, the trapped defect states are smaller in the GT sample, which is experimentally depicted in the PL spectrum (see Fig. 1(d)). Furthermore, the distance of the Fermi level from the valence band decreases, which is also observed experimentally in the valence band spectra (see Fig. 2(f)). As N has one electron less than O, it acts as an acceptor. Furthermore, from Fig. 3(d), we can see that the Fermi level (fixed at 0 eV) in *N*-substituted Ga_2O_3 has shifted inside the valence band, indicating the availability of free holes. Therefore, in the case of the GT sample, we have a lower n^{--} character, leading to a decrease in the persistent photoconductivity and enhancing the response of the photodetector device.

Next, we fabricated MSM PDs to compare the photo response quality of the PLD-grown Ga_2O_3 GS and GT samples [Fig. S4, ESI†]. The photoresponse results reveal that the GT device can detect light in a broad UV region varying from the UV C to UV A region of the wavelength spectrum with a higher photoresponse than the GS device, as presented in Fig. S4(d) (ESI†).

Furthermore, to make an ultra-broadband PD, we have utilized a vdW 2D/3D heterostructure by depositing a $MoSe_2$ thin film *via* magnetron sputtering on PLD-grown Ga_2O_3 GS

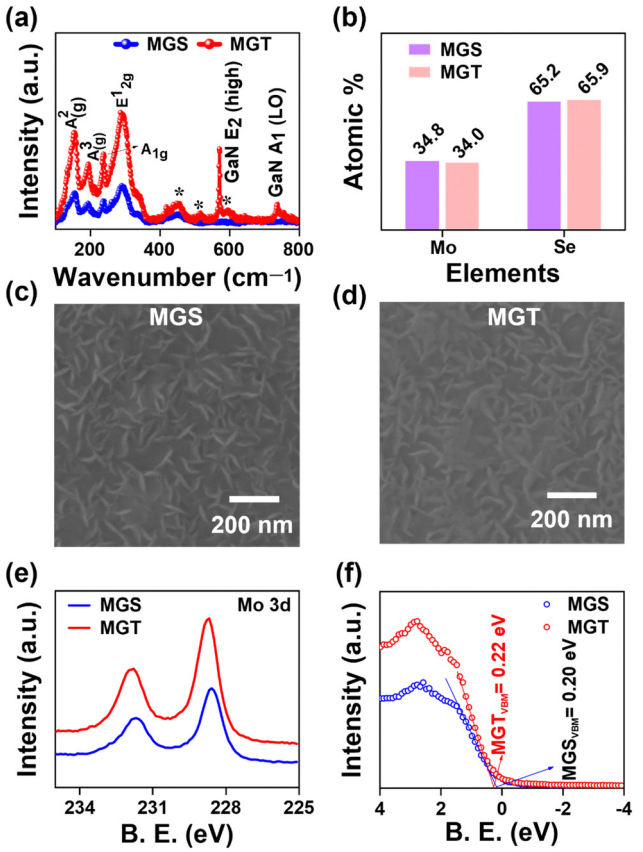

Fig. 4 (a) Raman spectra, (b) EDS atomic percentage, (c) and (d) plane view FESEM images, (e) XPS Mo 3d core level scan, and (f) valence band spectra of the MGS and MGT samples.

and GT samples and named them MGS and MGT, respectively. Fig. 4(a) displays the Raman spectra of MGS and MGT in the 100 to 800 cm^{-1} range. In Fig. 4(a), the presence of distinctive A_{1g} and E^1_{2g} phonon modes at Raman shifts of 236.1 (237.2) and 289.8 (286.5) cm^{-1}, respectively, are the signature Raman peaks of $MoSe_2$, which confirm the formation of $MoSe_2$ on the GS (GT) sample.[54] Furthermore, the Raman peaks at locations 155.2 (154.1) and 193.0 (194.1) cm^{-1} are assigned to the $A^2_{(g)}$ and $A^3_{(g)}$ modes of β-Ga_2O_3 in the MGS (MGT) sample, and the Raman peaks marked with asterisks correspond to the sapphire substrate.[39,41] In addition, the sharp and high-intensity Raman peaks recorded at 568.1 and 737.2 cm^{-1} in the MGT sample are attributed to the E_2 (high) and A_1 (LO) phonon modes of GaN.[44] Furthermore, to determine the atomic ratio of the sputtered $MoSe_2$ thin film, EDS elemental analysis was performed. Fig. 4(b) represents the graph of the atomic percentage of the elements present in the $MoSe_2$ thin film. The atomic ratio of 1 : 1.98 of Mo and Se revealed a suitable stoichiometry after the post-selenization of the magnetron-sputtered $MoSe_2$ thin film. Furthermore, the morphology of the MGS and MGT samples was examined by performing high-magnification FESEM image scans, as shown in Fig. 4(c) and (d). The FESEM images of $MoSe_2$ grown on PLD-grown Ga_2O_3 confirm the formation of worm-like structures of magnetron-sputtered $MoSe_2$ thin film, with uniform coverage over the entire scanned sample surfaces. The magnetron-sputtered TMD thin films were seen to have worm-like surface morphology because they first grow in a vertical direction. After reaching a specific thickness, their growth occurs in a lateral direction, forming worm-like structures.[55] Furthermore, to examine the surface roughness of the magnetron sputtered $MoSe_2$ thin film deposited on the PLD-grown β-Ga_2O_3 samples, we conducted AFM scans, as shown in Fig. S5(a) and (b) (ESI†).

The AFM imaging also compliments the worm-type $MoSe_2$ morphology, as shown in Fig. 4(c) and (d). The roughness of the MGS and MGT samples was estimated to be 7.37 and 5.42 nm, respectively. The low roughness value of MGT reveals a smoother surface than that of MGS. We conducted an XPS measurement of the Mo and Se core levels to study the chemical composition of the as-grown $MoSe_2/Ga_2O_3$ MGS and MGT samples. The core level Mo 3d and Se 3d scans for the MGS and MGT samples are presented in Fig. 4(e). The two broad peaks in the MGS and MGT samples are noticed to be shifted by a small value of binding energy. To determine the valence state of each element, we further deconvoluted it with a Voigt function and Sherley background. Fig. S6(a) and (b) (ESI†) show deconvoluted Mo 3d core level spectra presenting different valence states of Mo element present on the surface of the MGS and MGT samples, respectively. It shows the apparent appearance of Mo and Se on the surface of the $MoSe_2$ film and confirms the formation of the 2H-$MoSe_2$ phase.[56,57] The Voigt function fitted Se 3d spectra of the MGS and MGT samples are illustrated in Fig. S6(c) and (d) (ESI†). The peak position and FWHM of each deconvoluted peak are presented in Table S1 (ESI†). Furthermore, no peak corresponding to Mo–Ga or Se–Ga was observed in the XPS spectra of the MGS and MGT samples [Fig. S6, ESI†], which suggests that $MoSe_2$ is not attached to Ga_2O_3 by any chemical bonding but rather by weak van der Waals forces. Furthermore, the valence band maxima (VBM) calculated in the MGS and MGT samples are 0.20 and 0.22 eV, respectively [Fig. 4(f)], which reveals that the Fermi levels have nearly identical energy in both the $MoSe_2$ samples.

Furthermore, to study the photodetection properties of these heterostructures, we fabricated single and dual junction photodetector devices on $MoSe_2$/n-Ga_2O_3/sapphire (MGS) and $MoSe_2$/n-Ga_2O_3/p-GaN (MGT), respectively. A typical *I–V* curve of the hybrid MGS and MGT device was performed for −10 to 10 V, as presented in Fig. S7(a) and (b) (ESI†), respectively. To understand the photodetection properties of the fabricated devices at different wavelength regions of the electromagnetic spectrum, we have determined the time–dependent current (*I–t*) characteristics. The *I–t* characteristics were conducted at various applied biases from 0.5 to 10 V with laser light ON and OFF cycles taken to be 10 s. Fig. 5 shows the MGS device's *I–t* characteristics curve measurements under 255 nm and 1064 nm illumination. Fig. 5(a) displays the *I–t* curves at 255 nm laser illumination at various voltages of 0.5 to 10 V. The current is enhanced with a rise in externally applied voltage, as discussed in the previous section, and the cycles are repeatable and stable over multiple cycles of light ON and

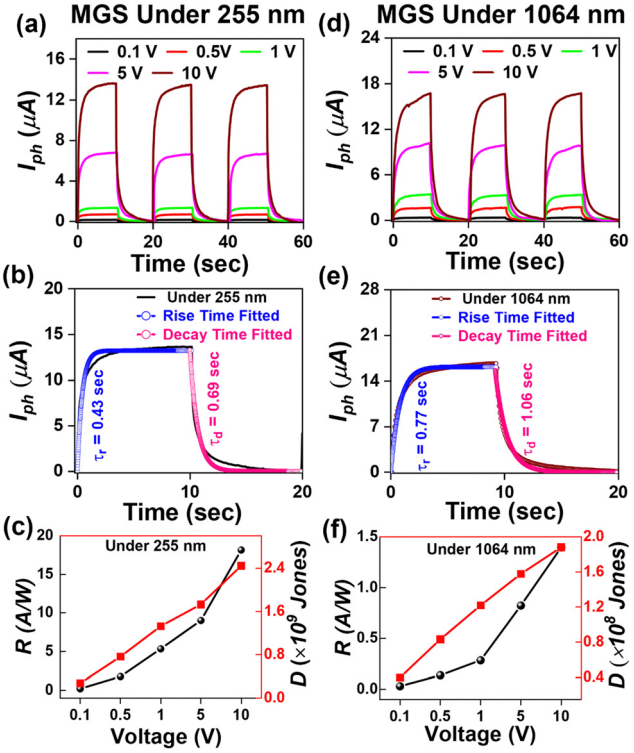

Fig. 5 The MGS device's (a) transient (*I*–*t*) photo response curve, (b) fitted time response curve, and (c) the responsivity and detectivity *versus* voltage graph of MGS under 255 nm illumination. The (d) transient (*I*–*t*) photo response curve, (e) fitted time response curve, and (f) the responsivity and detectivity *versus* voltage graph of MGS under 1064 nm illumination.

OFF. The photocurrent was seen to rise and become stable when the laser was illuminated quickly. After removing the laser light, the photocurrent reached its minimum value, which revealed that the device had a faster response time. The response (τ_r) and decay (τ_d) times of the device are estimated by fitting using the following equations:

$$I_{ph}(\tau) = I_0\left(1 - e^{\frac{-\tau}{\tau_r}}\right) \quad (1)$$

$$I_{ph}(\tau) = I_0 e^{\frac{-\tau}{\tau_d}} \quad (2)$$

where $I_{ph}(\tau)$ is the photocurrent at any time τ, and τ_r and τ_d are the rise and decay times, respectively. The rise and decay time values under 255 nm laser illumination estimated at 10 V are 0.43 s and 0.69 s, respectively, as shown in Fig. 5(b).

Furthermore, the performance of a photodetector is evaluated using photodetection parameters such as responsivity and detectivity. The values of these performance parameters were estimated using the following equations:

$$\text{Responsivity } (R) = \frac{I_{ph}}{P_{in} \times A} \quad (3)$$

$$\text{Detectivity } (D) = R \times \sqrt{\frac{A}{2eI_d}} \quad (4)$$

where, P_{in} is the incident optical power, A is the device's active area, and I_d is the device's dark current. Fig. 5(c) shows the graph of responsivity and detectivity of the MGS device under the illumination of 255 nm at various applied external voltages. The values of responsivity and detectivity at 10 V were estimated to be 18.1 A W^{-1} and 2.4 × 10^9 Jones, respectively, as presented in Table 2.

Furthermore, the MGS device underwent *I*–*t* curve measurements with 1064 nm laser light illumination, as shown in Fig. 5(d). The device's maximum current was measured at a voltage of 10 V to be 16.8 μA. The rise and decay time of the MGS device under the illumination of 1064 nm laser light was estimated using eqn (1) and (2), as shown in Fig. 5(e), and the values of rise and decay times are estimated to be 0.77 s and 1.06 s, respectively. It can be seen that the MGS device shows a similar time response under different laser light illumination. Furthermore, the responsivity and detectivity of the MGS device under 1064 nm laser light were estimated at various applied biases using eqn (3) and (4) and plotted in Fig. 5(f). The estimated values of responsivity and detectivity at 10 V were 1.4 A W^{-1} and 1.8 × 10^8 Jones, respectively. The values of the figures of merit of the MGS device under 1064 nm light illumination are displayed in Table 2.

It was observed from the spectral response in Fig. S4(d) (ESI†) that the introduction of p-GaN not only enhances the response of the device in DUV regions but also broadens the range of photodetection in UV regions due to the active GaN semiconducting material, which responds in the UV A region. Hence, photo response *I*–*t* curve measurements for the MGT device were performed at different laser wavelengths, as shown in Fig. 6. Fig. 6(a) shows the *I*–*t* curve of the MGT device under multiple ON/OFF cycles of laser illumination at wavelengths of 255 nm and 355 nm at a low voltage of 0.1 V. The photocurrent measured under wavelengths of 255 and 355 nm was 0.25 and 0.15 μA, respectively. Next, Fig. 6(b) displays the *I*–*t* curve of the MGT device under wavelengths of 255 nm and 355 nm at voltages varying from 0.5 to 10 V. The maximum photocurrent measured at 10 V of externally applied voltage is 25 μA. The value of photocurrent corresponding to the MGT device was

Table 2 Photo response parameters of the MGS and MGT devices were calculated at 10 V of externally applied bias under different wavelengths of laser illuminations

	Under 255 nm			Under 355 nm			Under 1064 nm		
Device	Responsivity (A W^{-1})/ detectivity (×10^9 Jones)	Response time (s) Rise (τ_r)	Decay (τ_d)	Responsivity (A W^{-1})/ detectivity (×10^9 Jones)	Response time (s) Rise (τ_r)	Decay (τ_d)	Responsivity (A W^{-1})/ detectivity (×10^9 Jones)	Response time (s) Rise (τ_r)	Decay (τ_d)
MGS	18.1/2.4	0.43	0.69	—	—	—	1.4/0.2	0.77	1.06
MGT	32.7/3.2	0.55	0.76	25.2/2.7	0.68	0.81	5.5/0.5	1.21	1.24

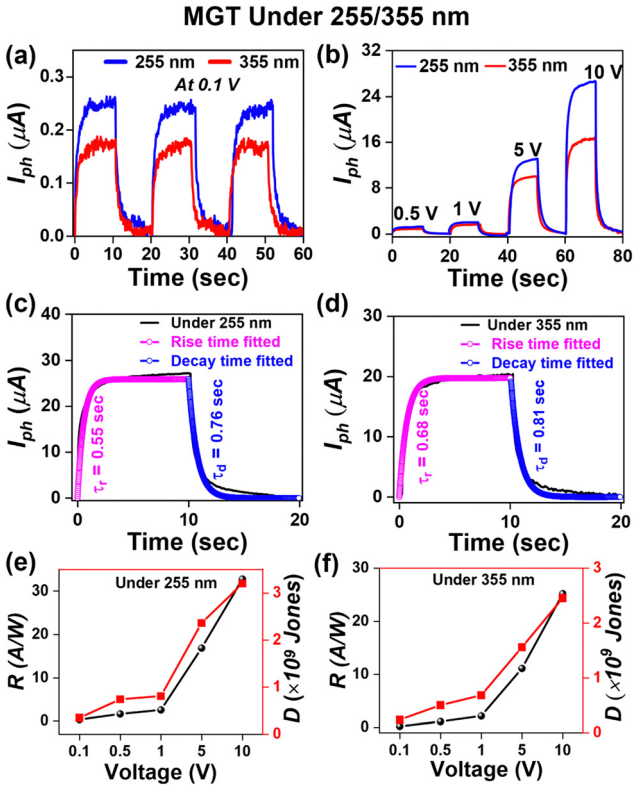

Fig. 6 MGT: transient (*I*–*t*) photo response curve under 255 and 355 nm laser illuminations at (a) 0.1 V and (b) 0.5–10 V. (c) and (d) Fitted time response curves and (e) and (f) responsivity and detectivity *versus* voltage graphs of MGT under 255 and 355 nm laser illuminations, respectively.

nearly double that of the MGS device at the same parameters under 255 nm laser illumination. This enhancement in responsivity of the MGT device as compared to MGS is due to the presence of p-GaN over the sapphire (0001), which boosts the photocurrent by nearly 100% because here both Ga_2O_3 and GaN are active materials in response to 255 nm laser light. Additionally, the photocurrent of the MGT device under 355 nm wavelength illumination was 17 μA at 10 V, which is lower than that measured under a 255 nm laser because only GaN is an active material for 355 nm laser light, unlike at 255 nm. Furthermore, the time response was calculated using eqn (1) and (2) for the MGT device under 255 and 355 nm light illumination and displayed in Fig. 6(c) and (d), respectively. The estimated values of rise and decay time are 0.55 (0.68) s and 0.76 (0.81) s, respectively, under 255 (355) nm laser illumination. The responsivity and detectivity of the MGT device were calculated at various applied voltages under 255 nm laser light illumination and plotted as shown in Fig. 6(e). The responsivity and detectivity estimated values at 10 V are 32.7 A W^{-1} and 3.2×10^9 Jones, respectively. Furthermore, the responsivity and detectivity calculated under 355 nm light illumination at various applied biases are shown in Fig. 6(f). The responsivity and detectivity measured at 10 V are 25.2 A W^{-1} and 2.7×10^9 Jones, respectively. The values of various figures of merit of the MGT device are presented in Table 2. In our work, we have found that the responsivity of PD devices is higher compared to the ones that have been recently fabricated using UWBG semiconductors.[17,39,58–64] A comparison table of our work with other studies is presented in Table 3.

Furthermore, the MGT device was characterized using 1064 nm laser light. Fig. 7(a) shows the *I*–*t* curve at a low voltage of 0.1 V. Fig. 7(b) shows the *I*–*t* curves at various applied biases ranging from 0.5 to 10 V. The maximum photocurrent was observed to be 65 μA at 10 V, which is four times higher than that observed for MGS under the same parameters and illumination of the same laser. This 4-fold enhancement in photocurrent of the MGT device reveals the significance of the presence of p-GaN. Fig. 7(c) shows the fitted time response of the MGT device under 1064 wavelength laser illumination, and the fitted value of the rise and decay times was calculated to be 1.21 and 1.24 s, respectively. Furthermore, the voltage-dependent graph of estimated responsivity and detectivity of the MGT device under 1064 nm is shown in Fig. 7(d), and the maximum responsivity found at 10 V is 5.5 A W^{-1} and 5.4×10^8 Jones, respectively. It was observed that the photoresponsivity of the MGT device is higher than that of the MGS device at each region of the electromagnetic spectrum.

The mechanism of enhancement in the photoresponse characteristics of the MGT device compared to the MGS device is shown in Fig. 8. Fig. 8(a) and (b) represent the cross-sectional view of the GS and GT samples, respectively. It was revealed from the valence band spectra of the GS and GT samples that they have UID n^{++} and n^{--} characteristics, respectively, which were theoretically confirmed by DFT calculation. Therefore, a p–n^{--} type heterojunction is formed in the MGT device between Ga_2O_3 (n^{--}) and GaN (p). Further, it is well known

Table 3 A comparison of photo response properties of deep UV photodetectors based on ultrawide bandgap semiconductors reported in the literature with our work

Heterojunction	Growth technique	Responsivity	Ref.
n-Ga_2O_3/SiC	MBE	18 mA W^{-1}@−10 V	17
n-Ga_2O_3/p-GaN	Gallium evaporation in oxygen plasma	0.18 A W^{-1}	39
AlGaN	MOCVD	0.19 A W^{-1}@−5 V	59
n-Ga_2O_3/ZnO	Magnetron sputtering	0.35 A W^{-1}@5 V	60
n-Ga_2O_3/GaN	CVD	27.5 mA W^{-1}@10 V	61
Amorphous Ga_2O_3/PET	Magnetron sputtering	8.9 A W^{-1}@15 V	62
MgZnO	MOCVD	100 mA W^{-1}@30 V	63
p-Ga_2O_3/n-GaN	Thermal oxidation	56 A W^{-1}@−5 V	64
n-Ga_2O_3/p-GaN	PLD	32.7 A W^{-1} at 10 V	This work

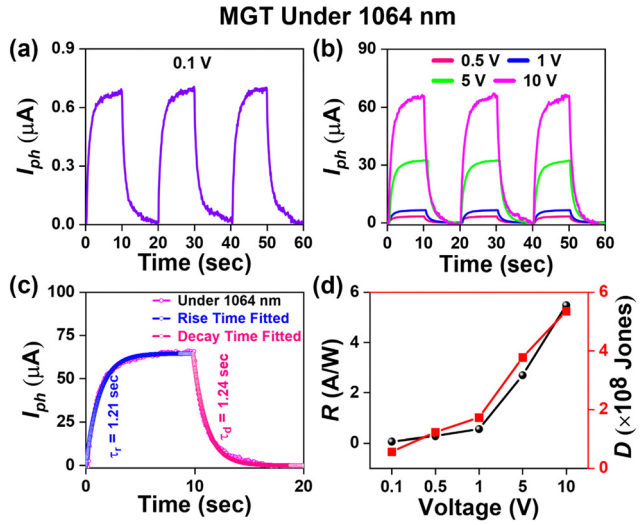

Fig. 7 MGT: transient (I–t) photo response curve at (a) 0.1 V and (b) 0.5–10 V, (c) fitted time response curve, and (d) responsivity and detectivity *versus* voltage graph of MGT under 1064 nm illumination.

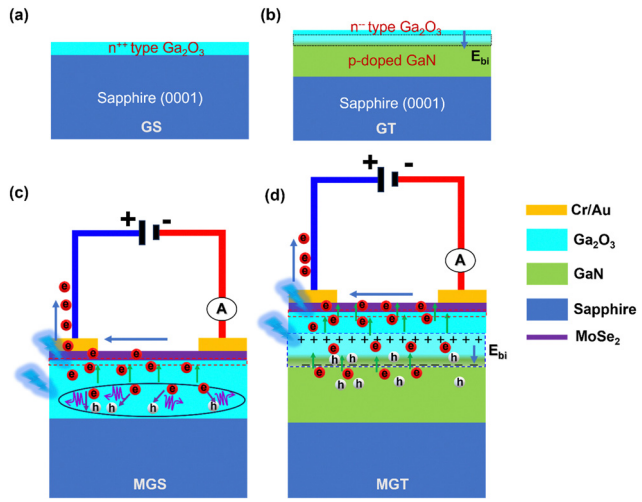

Fig. 8 Schematic diagram of the space charge region formed at the interface of the (a) GS and (b) GT samples. Charge transport mechanism under the illumination of (c) MGS and (d) MGT devices.

that if we join a low-doped semiconductor with a high-doped material, the depletion region or space charge region will be more on the low-doped semiconductor side. In the GS sample, Ga_2O_3 is not attached to any doped semiconductor; in the GT sample, it is grown on a p-type doped GaN semiconductor. Hence, the built-in electric field developed at the interface of the Ga_2O_3/GaN p–n^{--} junction will be spread over a large region on the Ga_2O_3 side (marked with a broken line region in black color) as shown in Fig. 8(b), while it is absent in the Ga_2O_3 GS sample.

Furthermore, Fig. 8(c) and (d) show the side views of the MGS and MGT devices, respectively. Fig. 8(c) shows that a built-in electric field is present at the interface of $MoSe_2$ and n-Ga_2O_3 due to the charge transfer in each other. Therefore, electron–hole pairs are generated in both semiconductors when the light is incident on the MGS device with $h\nu > E_g$ (Ga_2O_3). In an externally applied field, electrons drift toward the electrode from both the semiconductors.

However, it was observed that the built-in-electric field is present at the interface under the influence of which some of the charge carriers from Ga_2O_3 drift towards electrodes through $MoSe_2$. However, the electrons buried under some thickness near the bottom of the Ga_2O_3 semiconductor cannot reach the electrode. Instead, they recombine with the hole and annihilate as the built-in electric field is insufficient to drift them toward electrodes, as represented by a circle in Fig. 8(c), which limits the photoresponse properties of the GS sample.

Moreover, in Fig. 8(d), in addition to the built-in electric field developed at the interface due to the vdW heterostructure between $MoSe_2$ and n-Ga_2O_3, there is an extra built-in electric field present at the interface of the UID n^{--} Ga_2O_3 and p-doped GaN template. This extra electric field in the MGT device pushes these buried electrons in Ga_2O_3 to reach their respective electrodes without undergoing recombination with the photogenerated holes, and the diminished recombination of photogenerated charge carriers leads to improvement in photocurrent in the external circuit. Furthermore, the MGT device demonstrated higher photoresponse properties and exhibited a higher responsivity in the UV A region under 355 nm light illumination compared with MGS. Furthermore, the MGT device shows over four times higher photocurrent than MGS when illuminated with 1064 nm light. This is evidence that the built-in electric field at the interface of n-Ga_2O_3 and p-GaN plays a supportive role in efficiently separating the photogenerated charge carriers, significantly improving the photo response properties of the MGT device. Furthermore, the better crystalline, optical, and structural qualities of Ga_2O_3/p-GaN lead to the higher photoresponse properties of the MGT device compared to MGS. In conclusion, dual junction photodetectors are more efficient and work in a wide range of electromagnetic spectra, which makes them useful for futuristic optoelectronic applications.

Conclusion

We have explored the photodetection properties of single and dual junction photodetectors fabricated using the heterostructure of $MoSe_2$ with a PLD-grown Ga_2O_3/sapphire (0001) and Ga_2O_3/p-GaN template. The HRXRD measurements revealed that the PLD-grown Ga_2O_3 samples have the most stable β-phase. It was observed that Ga_2O_3/p-GaN has better crystalline, optical, and structural qualities than Ga_2O_3/sapphire. An energy difference in the Fermi level from the valence band maxima revealed that Ga_2O_3 grown on sapphire and p-GaN have UID n^{++} and n^{--} semiconductor characteristics, respectively. This is possibly due to the *N*-substitution defect in the case of the GT sample, as inferred from the density functional theory calculations. The additional built-in electric field at the

interface of n-Ga_2O_3/p-GaN has enhanced its photoresponse properties and broadened the range of photodetection in the UV region from UV-C to UV-A. Furthermore, in the NIR region, the 4-fold enhancement in responsivity of the photodetector on $MoSe_2$/n-Ga_2O_3/p-GaN than on $MoSe_2$/Ga_2O_3/sapphire is evidence of the essential role of the built-in electric field present in the former device. Therefore, these dual junction photodetectors have potential applications in futuristic optoelectronic devices.

Author contributions

Vishnu Aggarwal: conceptualization, investigation, writing – original draft. Manish Kumar: theoretical investigation, writing – review & editing. Rahul Kumar: data curation, visualization. Sudhanshu Gautam: methodology, formal analysis. Aditya Yadav: formal analysis, data curation. Shikha Srivastava: methodology. Anjana Dogra: resources, formal analysis. Govind Gupta: resources, formal analysis. Sumeet Walia: supervision, writing – review & editing. Sunil Singh Kushvaha: conceptualization, methodology, supervision, writing – review & editing.

Data availability

Data underlying the results may be obtained from the authors upon reasonable request.

Conflicts of interest

There are no conflicts to declare.

Acknowledgements

The authors thank the Director, CSIR-NPL, for his constant support and encouragement. The Science and Engineering Research Board funded this work under the Early Career Research Award Scheme, India (ECR/2017/001852). The authors express their gratitude to Dr R. Ganesan, Ms S. Sharma, Ms Simran Nehra, Dr Sandeep Singh, and Dr Jai Tawale for their assistance with sample characterization. V. A. and S. G. acknowledge CSIR for their senior research fellowships, and R. K. acknowledges the UGC for his senior research fellowship award.

References

1 Z. Li, T. Yan and X. Fang, Low-dimensional wide-bandgap semiconductors for UV photodetectors, *Nat. Rev. Mater.*, 2023, **8**(9), 587.
2 H. Yu, R. Wang, M. H. Memon, Y. Luo, S. Xiao, L. Fu and H. Sun, Highly Responsive Switchable Broadband DUV-NIR Photodetector and Tunable Emitter Enabled by Uniform and Vertically Grown III–V Nanowire on Silicon Substrate for Integrated Photonics, *Small*, 2024, **20**(10), 2307458.
3 D. Wang, X. Liu, Y. Kang, X. Wang, Y. Wu, S. Fang, H. Yu, M. H. Memon, H. Zhang, W. Hu, Z. Mi, L. Fu, H. Sun and S. Long, Bidirectional photocurrent in p–n heterojunction nanowires, *Nat. Electron.*, 2021, **4**(9), 645.
4 X. Deng, Z. Li, F. Cao, E. Hong and X. Fang, Woven Fibrous Photodetectors for Scalable UV Optical Communication Device, *Adv. Funct. Mater.*, 2023, **33**(23), 2213334.
5 A. F. Zhou, R. Velázquez, X. Wang and P. X. Feng, Nanoplasmonic 1D diamond UV photodetectors with high performance, *ACS Appl. Mater. Interfaces*, 2019, **11**(41), 38068.
6 J. Xu, W. Zheng and F. Huang, Gallium oxide solar-blind ultraviolet photodetectors: a review, *J. Mater. Chem. C*, 2019, **7**(29), 8753.
7 Y. Duan, S. Zhang, M. Cong, D. Jiang, Q. Liang and X. Zhao, Performance modulation of a MgZnO/ZnO heterojunction flexible UV photodetector by the piezophototronic effect, *J. Mater. Chem. C*, 2020, **8**(37), 12917.
8 D. Li, W. Gao, X. Sun, H. Yu, C. Liu and H. Yin, Direct Growth of Hexagonal Boron Nitride Thick Films on Dielectric Substrates by Ion Beam Assisted Deposition for Deep-UV Photodetectors, *Adv. Opt. Mater.*, 2021, **9**(12), 2100342.
9 H. Zhang, F. Liang, K. Song, C. Xing, D. Wang, H. Yu, C. Huang, Y. Sun, L. Yang, X. Zhao, H. Sun and S. Long, Demonstration of AlGaN/GaN-based ultraviolet phototransistor with a record high responsivity over 3.6×10^7 A W^{-1}, *Appl. Phys. Lett.*, 2021, **118**(24), 242105.
10 A. BenMoussa, A. Soltani, U. Schühle, K. Haenen, Y. M. Chong, W. Zhang, R. Dahal, J. Lin, H. Jiang and H. Barkad, Recent developments of wide-bandgap semiconductor based UV sensors, *Diamond Relat. Mater.*, 2009, **18**(5–8), 860.
11 T. Zhang, M. Li, J. Chen, Y. Wang, L. Miao, Y. Lu and Y. He, Multi-component ZnO alloys: bandgap engineering, heterostructures, and optoelectronic devices, *Mater. Sci. Eng., R*, 2022, **147**, 100661.
12 I.-H. Lee, T. G. Kim and Y. Park, Growth of crack-free AlGaN film on high-temperature thin AlN interlayer, *J. Cryst. Growth*, 2002, **234**(2–3), 305.
13 D. Kaur and M. Kumar, A strategic review on gallium oxide based deep-ultraviolet photodetectors: recent progress and future prospects, *Adv. Opt. Mater.*, 2021, **9**(9), 2002160.
14 U. Varshney, N. Aggarwal and G. Gupta, Current advances in solar-blind photodetection technology: using Ga_2O_3 and AlGaN, *J. Mater. Chem. C*, 2022, **10**(5), 1573.
15 D. Guo, Q. Guo, Z. Chen, Z. Wu, P. Li and W. Tang, Review of Ga_2O_3-based optoelectronic devices, *Mater. Today Phys.*, 2019, **11**, 100157.
16 J. Zhang, S. Han, M. Cui, X. Xu, W. Li, H. Xu, C. Jin, M. Gu, L. Chen and K. H. Zhang, Fabrication and interfacial electronic structure of wide bandgap NiO and Ga_2O_3 p–n heterojunction, *ACS Appl. Electron. Mater.*, 2020, **2**(2), 456.
17 J. Yu, L. Dong, B. Peng, L. Yuan, Y. Huang, L. Zhang, Y. Zhang and R. Jia, Self-powered photodetectors based on β-Ga_2O_3/4H-SiC heterojunction with ultrahigh current on/off ratio and fast response, *J. Alloys Compd.*, 2020, **821**, 153532.
18 Z. Cai, X. He, K. Wang, X. Hou, Y. Mei, L. Ying, B. Zhang and H. Long, Enhancing Performance of GaN/Ga_2O_3 P–N

Junction Uvc Photodetectors via Interdigitated Structure, *Small Methods*, 2023, 2301148.

19 Z. Lv, S. Yan, W. Mu, Y. Liu, Q. Xin, Y. Liu, Z. Jia and X. Tao, A High Responsivity and Photosensitivity Self-Powered UV Photodetector Constructed by the CuZnS/Ga_2O_3 Heterojunction, *Adv. Mater. Interfaces*, 2023, **10**(5), 2202130.

20 M. Deng, Z. Li, X. Deng, Y. Hu and X. Fang, Wafer-scale heterogeneous integration of self-powered lead-free metal halide UV photodetectors with ultrahigh stability and homogeneity, *J. Mater. Sci. Technol.*, 2023, **164**, 150.

21 P. Vashishtha, I. H. Abidi, S. P. Giridhar, A. K. Verma, P. Prajapat, A. Bhoriya, B. J. Murdoch, J. O. Tollerud, C. Xu, J. A. Davis, G. Gupta and S. Walia, CVD-Grown Monolayer MoS_2 and GaN Thin Film Heterostructure for a Self-Powered and Bidirectional Photodetector with an Extended Active Spectrum, *ACS Appl. Mater. Interfaces*, 2024, **16**(24), 31294.

22 D. Wang, W. Wu, S. Fang, Y. Kang, X. Wang, W. Hu, H. Yu, H. Zhang, X. Liu, Y. Luo, J.-H. He, L. Fu, S. Long, S. Liu and H. Sun, Observation of polarity-switchable photoconductivity in III-nitride/MoS_x core–shell nanowires, *Light: Sci. Appl.*, 2022, **11**(1), 227.

23 E. Hong, Z. Li, X. Zhang, X. Fan and X. Fang, Deterministic Fabrication and Quantum-Well Modulation of Phase-Pure 2D Perovskite Heterostructures for Encrypted Light Communication, *Adv. Mater.*, 2024, **36**(29), 2400365.

24 X. Zhang, Z. Li, T. Yan, L. Su and X. Fang, Phase-Modulated Multidimensional Perovskites for High-Sensitivity Self-Powered UV Photodetectors, *Small*, 2023, **19**(9), 2206310.

25 Y. Hu, Z. Li and X. Fang, Solution-prepared $AgBi_2I_7$ thin films and their photodetecting properties, *J. Inorg. Mater.*, 2023, **38**(9), 1055.

26 D. Wu, Z. Zhao, W. Lu, L. Rogée, L. Zeng, P. Lin, Z. Shi, Y. Tian, X. Li and Y. H. Tsang, Highly sensitive solar-blind deep ultraviolet photodetector based on graphene/$PtSe_2$/β-Ga_2O_3 2D/3D Schottky junction with ultrafast speed, *Nano Res.*, 2021, **14**(6), 1973.

27 R. Wadhwa, D. Kaur, Y. Zhang, A. Alexender, D. Kumar, P. Kumar, M. A. Namboothiry, Q. Qiao and M. Kumar, Fast response and high-performance UV-C to NIR broadband photodetector based on MoS_2/a-Ga_2O_3 heterostructures and impact of band-alignment and charge carrier dynamics, *Appl. Surf. Sci.*, 2023, **632**, 157597.

28 D. Monga and S. Basu, Tuning the photocatalytic/electrocatalytic properties of MoS_2/$MoSe_2$ heterostructures by varying the weight ratios for enhanced wastewater treatment and hydrogen production, *RSC Adv.*, 2021, **11**(37), 22585.

29 B. Peng, H. Zhang, H. Shao, Y. Xu, X. Zhang and H. Zhu, Thermal conductivity of monolayer MoS_2, $MoSe_2$, and WS_2: interplay of mass effect, interatomic bonding and anharmonicity, *RSC Adv.*, 2016, **6**(7), 5767.

30 Y. Ma, T. Chen, X. Zhang, W. Tang, B. Feng, Y. Hu, L. Zhang, X. Zhou, X. Wei and K. Xu, High-Photoresponsivity Self-Powered a-, ε-, and β-Ga_2O_3/p-GaN Heterojunction UV Photodetectors with an In Situ GaON Layer by MOCVD, *ACS Appl. Mater. Interfaces*, 2022, **14**(30), 35194.

31 U. Varshney, A. Sharma, P. Vashishtha, L. Goswami and G. Gupta, Ga_2O_3/GaN heterointerface-based self-driven broad-band ultraviolet photodetectors with high responsivity, *ACS Appl. Electron. Mater.*, 2022, **4**(11), 5641.

32 N. Zhang, Z. Lin, Z. Wang, S. Zhu, D. Chen, H. Qi and W. Zheng, Under-Seawater Immersion β-Ga_2O_3 Solar-Blind Ultraviolet Imaging Photodetector with High Photo-to-Dark Current Ratio and Fast Response, *ACS Nano*, 2024, **18**(1), 652.

33 P. Hohenberg and W. Kohn, Inhomogeneous electron gas, *Phys. Rev.*, 1964, **136**(3B), B864.

34 W. Kohn and L. J. Sham, Self-consistent equations including exchange and correlation effects, *Phys. Rev.*, 1965, **140**(4A), A1133.

35 J. P. Perdew, A. Ruzsinszky, G. I. Csonka, O. A. Vydrov, G. E. Scuseria, L. A. Constantin, X. Zhou and K. Burke, Restoring the density-gradient expansion for exchange in solids and surfaces, *Phys. Rev. Lett.*, 2008, **100**(13), 136406.

36 V. Blum, R. Gehrke, F. Hanke, P. Havu, V. Havu, X. Ren, K. Reuter and M. Scheffler, *Ab initio* molecular simulations with numeric atom-centered orbitals, *Comput. Phys. Commun.*, 2009, **180**(11), 2175.

37 X. Ma, R. Xu, Y. Mei, L. Ying, B. Zhang and H. Long, Crystalline anisotropy of β-Ga_2O_3 thin films on a c-plane GaN template and a sapphire substrate, *Semicond. Sci. Technol.*, 2022, **37**(3), 035003.

38 T. Oshima, T. Okuno and S. Fujita, Ga_2O_3 Thin Film Growth on c-Plane Sapphire Substrates by Molecular Beam Epitaxy for Deep-Ultraviolet Photodetectors, *Jpn. J. Appl. Phys.*, 2007, **46**(11R), 7217.

39 S. Nakagomi, T.-A. Sato, Y. Takahashi and Y. Kokubun, Deep ultraviolet photodiodes based on the β-Ga_2O_3/GaN heterojunction, *Sens. Actuators, A*, 2015, **232**, 208.

40 S. Nakagomi and Y. Kokubun, Crystal orientation of β-Ga_2O_3 thin films formed on c-plane and a-plane sapphire substrate, *J. Cryst. Growth*, 2012, **349**(1), 12.

41 V. Aggarwal, S. Gautam, A. Yadav, R. Kumar, B. K. Pradhan, B. S. Yadav, G. Gupta, S. K. Muthusamy, S. Walia and S. S. Kushvaha, Enhanced photoresponsivity in Bi_2Se_3 decorated GaN nanowall network-based photodetectors, *Mater. Res. Bull.*, 2024, **171**, 112608.

42 C. Kranert, C. Sturm, R. Schmidt-Grund and M. Grundmann, Raman tensor elements of β-Ga_2O_3, *Sci. Rep.*, 2016, **6**(1), 35964.

43 T. Yang, C. Shou, L. Xu, J. Tran, Y. He, Y. Li, P. Wei and J. Liu, Metal–Semiconductor–Metal Photodetectors Based on β-MgGaO Thin Films, *ACS Appl. Electron. Mater.*, 2023, **5**(4), 2122.

44 S. S. Kushvaha, M. S. Kumar, A. K. Shukla, B. S. Yadav, D. K. Singh, M. Jewariya, S. R. Ragam and K. K. Maurya, Structural, optical and electronic properties of homoepitaxial GaN nanowalls grown on GaN template by laser molecular beam epitaxy, *RSC Adv.*, 2015, **5**(107), 87818.

45 V. Aggarwal, C. Ramesh, U. Varshney, P. Tyagi, S. Gautam, A. K. Mauraya, B. S. Yadav, G. Gupta, R. Ganesan, M. S. Kumar and S. S. Kushvaha, Correlation of crystalline and optical properties with UV photodetector characteristics of

GaN grown by laser molecular beam epitaxy on a-sapphire, *Appl. Phys. A*, 2022, **128**(11), 989.

46 J. Wei, K. Kim, F. Liu, P. Wang, X. Zheng, Z. Chen, D. Wang, A. Imran, X. Rong and X. Yang, β-Ga_2O_3 thin film grown on sapphire substrate by plasma-assisted molecular beam epitaxy, *J. Semicond.*, 2019, **40**(1), 012802.

47 Y. Wang, Z. Lin, J. Ma, Y. Wu, H. Yuan, D. Cui, M. Kang, X. Guo, J. Su, J. Miao, Z. Shi, T. Li, J. Zhang, Y. Hao and J. Chang, Multifunctional solar-blind ultraviolet photodetectors based on p-PCDTBT/n-Ga_2O_3 heterojunction with high photoresponse, *InfoMat*, 2024, **6**(2), e12503.

48 Q. Shi, Q. Wang, D. Zhang, Q. Wang, S. Li, W. Wang, Q. Fan and J. Zhang, Structural, optical and photoluminescence properties of Ga_2O_3 thin films deposited by vacuum thermal evaporation, *J. Lumin.*, 2019, **206**, 53.

49 B. R. Tak, S. Dewan, A. Goyal, R. Pathak, V. Gupta, A. K. Kapoor, S. Nagarajan and R. Singh, Point defects induced work function modulation of β-Ga_2O_3, *Appl. Surf. Sci.*, 2019, **465**, 973.

50 S. K. Jain, P. Goel, U. Varshney, T. Garg, N. Aggarwal, S. Krishna, S. Singh and G. Gupta, Impact of thermal oxidation on the electrical transport and chemical & electronic structure of the GaN film grown on Si and sapphire substrates, *Appl. Surf. Sci. Adv.*, 2021, **5**, 100106.

51 K.-J. Gan, P.-T. Liu, T.-C. Chien, D.-B. Ruan and S. M. Sze, Highly durable and flexible gallium-based oxide conductive-bridging random access memory, *Sci. Rep.*, 2019, **9**(1), 14141.

52 C. Ramesh, P. Tyagi, V. Aggarwal, S. Pal, S. Dhua, M. Singh, P. Pal, S. C. Roy, S. P. Singh, S. K. Muthusamy and S. S. Kushvaha, Hybrid Reduced Graphene Oxide/GaN Nanocolumns on Flexible Niobium Foils for Efficient Photoelectrochemical Water Splitting, *ACS Appl. Nano Mater.*, 2023, **6**(3), 1898.

53 M. Higashiwaki, β-Ga_2O_3 material properties, growth technologies, and devices: a review, *AAPPS Bull.*, 2022, **32**(1), 3.

54 R. Kumar, V. Aggarwal, S. Gautam, B. K. Pradhan, R. K. Mukherjee, M. Senthil Kumar and S. S. Kushvaha, Growth of 2D MoS_2 and $MoSe_2$ layers for photodetector application, *Mater. Today: Proc.*, 2023, DOI: **10.1016/j.matpr.2023.04.407**.

55 Z.-M. Wang, C.-B. Yao, L.-Y. Wang, X. Wang, C.-H. Jiang and S.-B. Yang, Interfacial charge transfers and carrier regulation characteristics of narrow/wide band gap TMDs@Ga_2O_3 n–n heterojunction film, *J. Alloys Compd.*, 2022, **915**, 165286.

56 S. Kandar, K. Bhatt, N. Kumar, A. K. Kapoor and R. Singh, Nanoscale $MoSe_2$ Grown on Si(111) for Potential Applications in Broadband Photodetectors, *ACS Appl. Nano Mater.*, 2024, **7**, 6736.

57 G. S. Papanai, K. R. Sahoo, S. Gupta and B. K. Gupta, Role of processing parameters in CVD grown crystalline monolayer $MoSe_2$, *RSC Adv.*, 2022, **12**(21), 13428.

58 X. Xie, Z. Zhang, B. Li, S. Wang, M. Jiang, C. Shan, D. Zhao, H. Chen and D. Shen, Mott-type $Mg_xZn_{1-x}O$-based visible-blind ultraviolet photodetectors with active anti-reflection layer, *Appl. Phys. Lett.*, 2013, **102**(23), 231122.

59 F. Xie, Y. Gu, Z. Hu, B. Yu and G. Yang, Ultra-low dark current back-illuminated AlGaN-based solar-blind ultraviolet photodetectors with broad spectral response, *Opt. Express*, 2022, **30**(13), 23756.

60 D. Guo, H. Shi, Y. Qian, M. Lv, P. Li, Y. Su, Q. Liu, K. Chen, S. Wang and C. Cui, Fabrication of β-Ga_2O_3/ZnO heterojunction for solar-blind deep ultraviolet photodetection, *Semicond. Sci. Technol.*, 2017, **32**(3), 03LT01.

61 W. Ding and X. Meng, High performance solar-blind UV detector based on β-Ga_2O_3/GaN nanowires heterojunction, *J. Alloys Compd.*, 2021, **866**, 157564.

62 Y. Chen, Y. Lu, M. Liao, Y. Tian, Q. Liu, C. Gao, X. Yang and C. Shan, 3D solar-blind Ga_2O_3 photodetector array realized via origami method, *Adv. Funct. Mater.*, 2019, **29**(50), 1906040.

63 X. H. Xie, Z. Z. Zhang, B. H. Li, S. P. Wang, M. M. Jiang, C. X. Shan, D. X. Zhao, H. Y. Chen and D. Z. Shen, Mott-type $Mg_xZn_{1-x}O$-based visible-blind ultraviolet photodetectors with active anti-reflection layer, *Appl. Phys. Lett.*, 2013, **102**(23), 231122.

64 Y. Han, Y. Wang, S. Fu, J. Ma, H. Xu, B. Li and Y. Liu, Ultrahigh Detectivity Broad Spectrum UV Photodetector with Rapid Response Speed Based on p-βGa_2O_3/n-GaN Heterojunction Fabricated by a Reversed Substitution Doping Method, *Small*, 2023, **19**(16), 2206664.